Tuning the Optoelectronic Properties of ZnO:Al by Addition of Silica for Light Trapping in High-Efficiency Crystalline Si Solar Cells

Ali Dabirian, Silvia Martin de Nicolas, Bjoern Niesen, Aïcha Hessler-Wyser, Stefaan De Wolf, Monica Morales-Masis, and Christophe Ballif*

Highly transparent electrodes with a well-tuned refractive index are essential for a wide range of optoelectronic devices, such as light emitting diodes and solar cells. Here, it is shown that the transparency of ZnO:Al can be improved and its refractive index can be reduced simultaneously by the addition of SiO_2 into the layer. It is found that for low SiO_2 concentrations, Si quenches oxygen vacancies and improves the layer transparency. At higher SiO_2 concentrations a highly transparent amorphous compound of Zn_xSi_yO:Al forms, with a refractive index that scales down with the relative Si/Zn ratio. These layers are tested in Si heterojunction solar cells by inserting them between Si and the metallic rear contact of such devices. A consistent improvement is found in the cell short-circuit current density and external quantum efficiency with increasing Si incorporation. Our findings establish a general strategy to tune the optical properties of transparent conductive oxides for improved light management in solar cells.

1. Introduction

Transparent conductive oxides (TCOs) play a key role in a wide range of optoelectronic devices such as touch-screens, light emitting diodes (LEDs), and photovoltaic (PV) solar cells. Key metrics of TCOs are their sheet resistance (R_{sh}) and transparency (T) where maximum transparency at low sheet resistance is desirable.[1] However, to maximize light in-coupling in single-junction [2–4] and multijunction[5] solar cells (or out-coupling from LEDs[6]), the refractive index of the TCOs also plays an important role and therefore the ability of tuning TCO refractive index is essential in achieving the optimal performance.

For crystalline silicon solar cells, the world-record power conversion efficiency was recently set at 25.6%, using silicon heterojunction (SHJ) technology, in an interdigitated contact design.[2] In a SHJ device, surface defects of c-Si are passivated by ultrathin intrinsic hydrogenated amorphous Si (a-Si:H) layers thus enabling open-circuit voltages as high as 750 mV.[2] The Ohmic losses between doped a-Si:H layers and metallic electrodes of the SHJ device are minimized by inserting a TCO layer in between. These TCO layers provide additional functionalities of antireflection in front of the cell[3] and the possibility of infrared (IR) light management in the cell rear-contact.[7–9]

Optical absorption in the IR induced by free carriers in TCOs can significantly deteriorate the generated photocurrent of the PV device.[10] These losses can be minimized by making the TCO more transparent often by reducing oxygen vacancies. However, this approach results in an increase of TCO refractive index, which is undesirable when the TCO is located at the rear of the device and covered by a metal layer. In such a case, the high refractive index of the TCO yields more efficient coupling to the surface plasmon polariton (SPP) modes of the metallic rear-contact, resulting in parasitic optical absorption losses.[7–9] Therefore, strategies that simultaneously reduce the refractive index and the IR absorption loss of TCOs are appealing in IR light management of c-Si solar cells, as well as in all devices incorporating a TCO/metal stack.

In this article, we propose the addition of SiO_2 to ZnO:Al as a strategy to synthesize highly transparent TCOs with a low refractive index. We evaluate the performance of these TCOs for IR light management in SHJ solar cells to minimize optical absorption losses in the TCO and the metallic rear-contact. We should mention that Si doping of ZnO-based TCOs has been studied in the context of thin film transistors (TFT) to either stabilize the TFT[11,12] or to improve the conductivity of the TCO.[13] Such studies have been primarily focused on a few percent concentrations of Si in ZnO where Si functions as an impurity doping. Our work addresses the refractive index tuning of ZnO:Al by SiO_2 addition in a range of concentrations wide enough to observe both electronic and structural modifications of ZnO:Al layers by addition of SiO_2. We synthesize ZnO:Al with different concentration of SiO_2 up to 52 mol% SiO_2 in a cosputtering process. We analyze the chemical and structural properties of the obtained compounds and classify whether SiO_2 affects the electronic or structural properties of the ZnO:Al

Dr. A. Dabirian, Dr. S. Martin de Nicolas,
Dr. B. Niesen, Dr. A. Hessler-Wyser,
Dr. S. De Wolf, Dr. M. Morales-Masis,
Prof. C. Ballif
Ecole Polytechnique Fédérale de Lausanne (EPFL)
Institute of Microengineering (IMT)
Photovoltaics and Thin-Film Electronics Laboratory
Rue de la Maladière 71, Neuchatel 2002, Switzerland
E-mail: ali.dabirian@epfl.ch

DOI: 10.1002/admi.201500462

© 2015 WILEY-VCH Verlag GmbH & Co. KGaA, Weinheim

layer. We relate the structural properties to the optoelectronic properties of these compounds where we observe the improvement in transparency, the tuning of refractive index, and the blue-shift in the optical absorption edge as the result of SiO_2 addition. Finally, we fabricate c-Si heterojunction solar cells integrating these new compounds. Compared to a standard ZnO:Al, we find a clear improvement in the cell's short-circuit current density, power conversion efficiency, and the IR external quantum efficiency as the result of optimal SiO_2 addition.

2. Results and Discussion

To synthesize ZnO:Al thin films with defined concentrations of SiO_2, we first calibrated the sputtering processes of ZnO:Al and SiO_2 individually. The layers were deposited from ZnO:Al (1.5 at% Al) and SiO_2 targets via reactive radio-frequency (RF) sputtering in a system with a maximum background pressure of 2×10^{-7} mbar at 1 µbar processing pressure. The Experimental Section provides a detailed description of the processing and characterization methods. The deposition rate of ZnO and SiO_2 films were determined versus the sputtering power densities in the range of 0.16–0.96 W cm^{-2} (**Figure 1**a). The deposition rate data were converted from nm/min to mol/min taking into account the molecular weight and density of the individual compounds. They were then used to process ZnO:Al layers with a targeted SiO_2 concentration in a codeposition process (Figure 1b).

X-ray photoelectron spectroscopy (XPS) was conducted to study the chemical composition of the layers and to determine

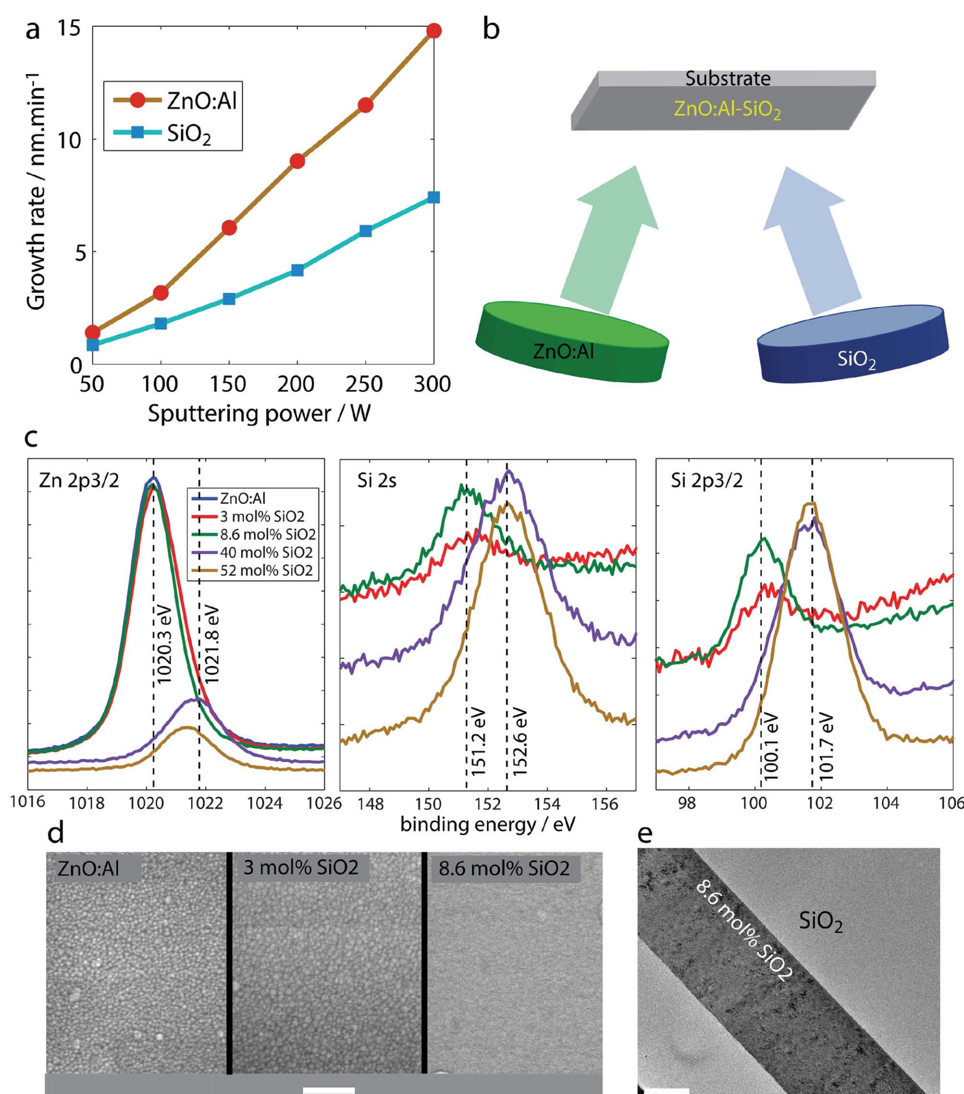

Figure 1. Material synthesis and structural characterizations. Panel a) shows the growth rate of individual ZnO:Al and SiO_2 layers versus sputtering power. Panel b) shows a schematic illustrating the sputtering configuration used for codeposition ZnO:Al and SiO_2. Panel c) shows the XPS spectra of the layers synthesized with different concentration of SiO_2 in ZnO:Al. Panel d) shows the top-view SEM images of the layers illustrating how the surface morphology of the ZnO:Al layers evolves by addition of SiO_2, the scale bar is 200 nm. Panel e) shows the dark-field TEM image of the cross-section of the ZnO:Al layer with 8.6 mol% SiO_2, the scale bar is 50 nm.

© 2015 WILEY-VCH Verlag GmbH & Co. KGaA, Weinheim

the chemical state of the elements present in the layer. The survey XPS spectra (Figure S1, Supporting Information) shows the crystal field splitting for Si *2p* and Zn *2p* orbitals and the high-resolution spectra (Figure 1c) show that in both cases no shoulder peak is present. These two observations confirm that Si and Zn are in Si^{4+} and Zn^{2+} oxidation states in the layers. In addition we did not observe the Al^{3+} peak due to its low content (<1.5 at%).[14] The samples that from the calibration were intended to have 5 and 10 mol% SiO_2 show 3 and 8.6 mol% SiO_2, respectively. The SiO_2 concentration, though slightly smaller than expected, is hence quite close to the predicted values from the process calibration. For higher targeted SiO_2 content, the measured values are significantly larger than the predicted values, i.e., those intended to have 20 and 33 mol% SiO_2 actually contain 40 and 52 mol% SiO_2. This effect is likely to occur due to the mutual interaction of the two sputtering sources which is linked to the configuration of the targets in the sputtering equipment.

We extract more information about the chemical state of Si and Zn in the layers by analyzing the relevant electron binding energies (BE). In the layers with 3 and 8.6 mol% SiO_2, the BE of the Zn^{2+} peak stays nearly at the same position as in pure ZnO:Al layers, i.e., BE = 1020.3 eV. However the position of the Si^{4+} peaks shifts significantly to lower BE relative to the pristine SiO_2 layers. The BE of Si $2p_{3/2}$ and Si *2s* in these layers is 100.1 and 151.2 eV instead of 103.4 eV and 154 eV in pristine SiO_2, respectively.[15] These features indicate that, at these low SiO_2 concentrations, only the BE of the Si–O bond is influenced by the presence of Zn atoms. This suggests that in these layers the interaction of SiO_2 and ZnO:Al is mostly an electronic interaction especially at the 3 mol% SiO_2 case where the film microstructure is not strongly influenced.[11,16]

At higher SiO_2 concentrations in ZnO:Al, the BEs of Si^{4+} peaks shift relative to the pristine SiO_2 but to a smaller extent. In addition, we observe that the BE of Zn^{2+} also shifts toward higher energies relative to the Zn^{2+} BE in ZnO:Al. These shifts indicate that the electron distribution of the Zn atoms is influenced by the presence of Si atoms and vice versa. Therefore we can conclude that, at these conditions, the layer is composed of an amorphous mixture of an $Al{:}Si_xZn_yO$ composition rather than a layer with separated ZnO:Al and SiO_2 phases. Similar observations and conclusions with detailed explanations were reported in other oxide mixtures such as Nb_2O_5-HfO_2,[17,18] and SiO_2-HfO_2.[19]

The ZnO:Al layers deposited on glass show a surface morphology composed of round-shape grains of 15–20 nm when observed with a scanning electron microscope (SEM) (Figure 1d). The addition of 3 mol% SiO_2 does not alter the surface morphology significantly. However, when 8.6 mol% SiO_2 is added, the layer exhibits a much smoother surface. The morphology remains then the same as more SiO_2 is added. This is a well-known feature of SiO_2 that it suppresses the crystallization when it is added to polycrystalline materials.[20]

Table 1. Electrical properties of the ZnO:Al layers doped with SiO_2.

Sample	R_{sh} [Ω sq^{-1}]	Mobility (μ) [cm2 V^{-1} s^{-1}]	Carrier density (n_e) [cm^{-3}]
ZnO:Al	265	9.35	2.55*e*+20
3 mol% SiO_2	410	6.58	2.33*e*+20
8.6 mol% SiO_2	58k	3.35	3.23*e*+18

The bright-field transmission electron microscopy (BF-TEM) image of the ZnO:Al layer with 8.6 mol% SiO_2 shows the presence of randomly oriented nanocrystals within the layer. These nanocrystals seem to be interconnected in an amorphous mixture of ZnO:Al and SiO_2 establishing an electrical conducting path through the layer (Figure S2, Supporting Information). The high-resolution TEM images show that these nanocrystals have interference fringes typical to crystalline materials. Since SiO_2 is not expected to crystallize under conditions studied here, we conclude that the nanocrystals are ZnO:Al. However we cannot comment on the presence of Si in the nanocrystals. X-ray diffraction (XRD) measurements carried out on the samples in Bragg–Brentano configurations (Figure S3, Supporting Information) show that the ZnO:Al sample is polycrystalline and textured along the ⟨001⟩ orientation. This is in agreement with structural characterizations reported in the Literature for ZnO:Al layers deposited by sputtering.[21,22] The addition of SiO_2 leads to broadening of the (002) peak and the reduction of its intensity. These observations both indicate that the size of the crystallites in the layers becomes smaller with the addition of SiO_2.

Table 1 lists the sheet resistance (R_{sh}), Hall-effect mobility (μ), and carrier density (n_e) of the layers with up to 8.6 mol% SiO_2. The layers with larger SiO_2 content were too resistive to be measured using the 4 point-probe and Hall-effect systems. Electronic properties of the layers, with 100 ± 5 nm thickness, show that the presence of 3 mol% SiO_2 slightly degrades the conductivity whereas addition of 8.6 mol% SiO_2 turns the layer into a highly resistive one.

Adding 3 mol% SiO_2 to ZnO:Al slightly degrades both the carrier density and the mobility. However the addition of smaller percentages (estimated <1 mol%) of SiO_2 (Table S1, Supporting Information) shows improvement in mobility and deterioration of carrier density. The reduction of free carriers is attributed to the so-called "oxygen getter" effect that takes place due to the stronger affinity of O to Si rather than Zn.[23] The mobility deterioration that we observe in the film with 3 mol% SiO_2 is likely due to microstructural modifications induced by the presence of SiO_2 in ZnO:Al. Although the "oxygen getter" effect and the slight microstructural changes both contribute to the changes in optical properties of this layer, we cannot draw conclusions on the extent of each effect with our current set of measurements.

When 8.6 mol% SiO_2 is added the mobility decreases further whereas the carrier density dramatically drops by three orders of magnitude. Also, from the SEM and TEM measurements (Figure 1e, and Figure S2, Supporting Information) we observe that the film microstructure is completely modified by the presence of 8.6 mol% SiO_2. Therefore these dramatic changes in electrical properties are likely linked to structural modification in the layer induced by addition of SiO_2. We should mention that a partial reduction of the density of oxygen vacancies in the ZnO nanocrystals can also play a role.

The optical transmittance and absorptance spectra of the samples measured by UV–vis spectroscopy (**Figure 2**a,b) both confirm that by adding SiO_2, i) the near-infrared (NIR) optical absorption decreases and hence the transmittance improves,

© 2015 WILEY-VCH Verlag GmbH & Co. KGaA, Weinheim

and ii) the optical absorption edge blue shifts. The NIR optical absorption in ZnO:Al is a sub-band gap absorption attributed to the presence of free carriers. Free carrier absorption, $A(\lambda)$, is proportional to the absorption cross-section, $\sigma(\lambda)$, layer thickness, L, and the carrier density, n_e: $A(\lambda) = n_e \bullet \sigma(\lambda) \bullet L$.[24] Therefore, improvement in NIR transparency can be directly related to the reduction of n_e in agreement with Hall-effect measurement results.

The blue-shift of the optical absorption edge is examined more accurately through the Tauc analysis. Such analysis assumes a relation between the optical absorption coefficient (α) and the photon energy which is $\alpha^2 \propto (E-E_g)$ for direct band gap and $\alpha \propto (E-E_g)^2$ for indirect band gap materials.[25,26] The parameter α is calculated from film thickness, t, transmittance, T, and reflectance, R, by[27]

$$\alpha = -\left(\frac{1}{t}\right)\ln\left(\frac{T}{1-R}\right). \tag{1}$$

The linear fit was only possible with α^2 versus photon energy, indicating that all the compounds have a direct band gap.[25] The band gap is determined by the intersection of the slope with the photon energy axis (inset of Figure 2b). We obtained E_g = 3.39 eV for ZnO:Al which gradually increases as more SiO_2 is added. The bandgap broadening is equivalent to the blue-shift of the optical absorption edge. This is a direct consequence of inclusion of the more transparent SiO_2 ($E_g \approx 9$ eV) into the ZnO:Al layer, which has been observed in other material systems.[17] The continuous blue-shift of the optical absorption edge with the addition of SiO_2 indicates in all cases studied here that the SiO_2 is uniformly mixed with ZnO:Al and separate phases do not form. This might be in contrarast to the presence of crystallites in ZnO:Al layer with 8.6 mol% SiO_2, however we should mention that it was not possible to characterize the crystallite and conclude on the presence or absence of SiO_2 in them. It is likely that in this case the presence of slightly less SiO_2 in the crystallite relative to the amorphous matrix makes it difficult to separate the two very close optical absorption edges.

The refractive index of the layers, $\eta = n + ik$, was obtained by numerically fitting the optical ellipsometry data with a combination of Tauc–Lorentz and Drude models for refractive indices.[9] The Tauc–Lorentz part models the UV and visible part of the spectrum in which the interband optical absorption takes place. The Drude model is applied predominantly in the IR and NIR (only in layers with high n_e) where free carrier absorption is strong. Our ellipsometry results of ZnO:Al layers show a close agreement with the Literature values for sputtered ZnO:Al layers in terms of the order of extinction coefficient (k) and the plasma frequency.[28] We further examine the results by dividing them in two categories: i) low SiO_2 content up to 8.6 mol% and ii) the ZnO:Al with 8.6 mol% SiO_2 content and larger SiO_2 content.

In layers with low SiO_2 content n dramatically increases with the addition of SiO_2 at $\lambda > 500$ nm whereas it slightly decreases at $\lambda < 500$ nm. The n at longer wavelengths is strongly influenced by free carriers whereas at $\lambda < 500$ nm it is solely influenced by bound electrons. The latter effect is due to the inclusion of the lower refractive index SiO_2 in the layer whereas the former effect is due to quenching free carrier by Si inclusion. The presence of free carriers manifests itself in the large k values, which decreases on addition of SiO_2.

The ZnO:Al layer with 8.6 mol% SiO_2 and more show small k values, which is a decreasing function of SiO_2 content. In addition n of these layers behaves as a slowly decreasing plateau at $\lambda > 500$ nm. This is due to the small plasma frequencies $[\omega_p^2 = n_e e^2/(\varepsilon_0 m^*)]$ of these layers relative to those of layers with lower SiO_2 content (inset of Figure 2d). This indicates that in these SiO_x rich layers, the refractive index at the wavelength range studied is determined by the bound electrons of the materials rather than the free electrons.

To provide a better reference for comparison we annealed ZnO:Al in air for 1 h at 500 °C and the sample turned

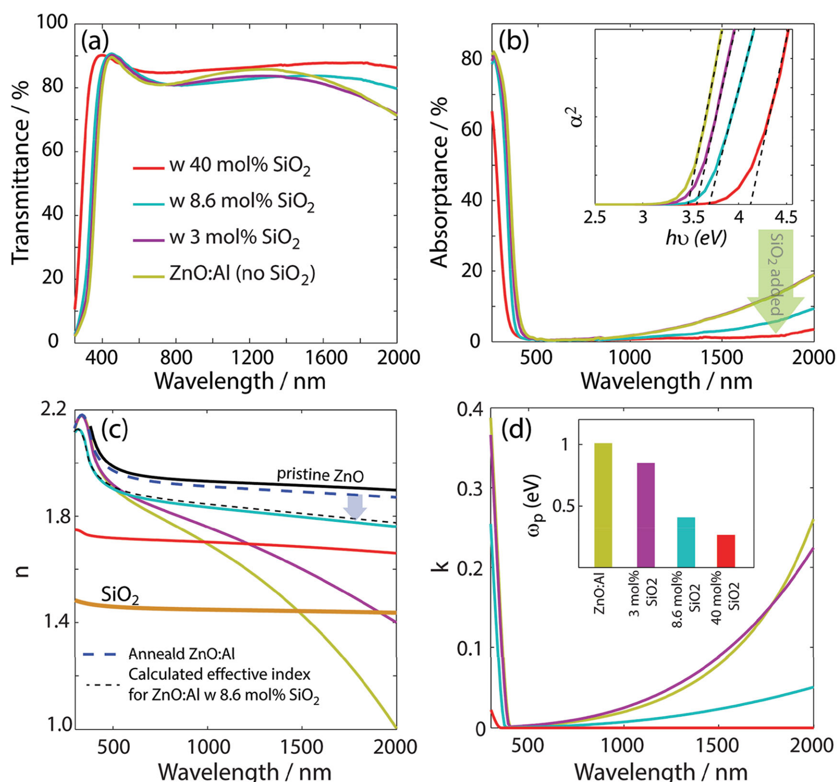

Figure 2. Optical properties. Panels a) and b) show the optical transmittance and absorptance of the ZnO:Al layers with different SiO_2 content measured by UV–vis spectrometer, respectively. The inset of panel b) is the Tauc plot of the optical absorption coefficients (α) used for estimation of the bandgap. Panels c) and d) show the real and imaginary parts of refractive index ($\eta = n + ik$) of these layers measured by spectroscopic ellipsometry. The dashed curve in panel c) is the refractive index calculated from effective medium theory for a mixture of 8.6 mol% SiO_2 in pristine ZnO. The inset of panel d) shows the plasma frequency (ω_p) of the layers extracted from the Drude model of refractive index.

© 2015 WILEY-VCH Verlag GmbH & Co. KGaA, Weinheim

completely resistive in agreement with previous reports.[29] Then we measured its refractive index and used it as the reference for comparison with refractive index of the samples with added SiO_2. Thus if we compare the n of the layers with 8.6 and 40 mol% SiO_2 with that of annealed ZnO:Al which is quite similar to pristine ZnO[30] we observe a consistent decrease in the n values with increasing SiO_2 molar fraction at 8.6 mol% and beyond. Within close agreement, this follows the effective refractive index that we can calculate for compounds formed as the homogeneous mixture of pristine SiO_2 and pristine ZnO by Maxwell–Garnett theory.[31] The dashed curve shows the calculated refractive index for ZnO containing 8.6 mol% SiO_2, showing an excellent agreement with the experimentally measured one with a slight discrepancy in the IR due to presence of small concentration of free carriers. The effective medium theory suggests the possibility of continuous tuning of the refractive index for a mixture of ZnO and SiO_2.[32] We should mention that this theory assumes no chemical interaction among the constituting oxides, therefore it is not directly applicable to the lower concentration of SiO_2 in ZnO:Al due to chemical interaction of SiO_2 and ZnO:Al appearing by quenching free carriers.

One possible application of these TCOs with improved transparency and low refractive index is in the rear-contact of SHJ solar cells.[7–9,33] In these cells the TCO is inserted between the Ag rear-contact and the doped a-Si:H layer to guarantee a low contact resistivity. Earlier, it was shown that the IR parasitic absorption losses in the rear-contact of these cells can be mitigated by lowering the free carrier density in the used TCO.[7–10] In addition, in case the metal contact is deposited as a blanket layer, an improved infrared response can be obtained by lowering the refractive index of the underlying films.[8] We tested our layers in such SHJ solar cells with textured substrates (250 µm thick, n-type c-Si wafers), in the configuration shown in **Figure 3**a. Several devices were obtained for each wafer, where the ITO front contact was defined by masked deposition, yielding areas slightly larger than 4 cm^2 for cell fabrication (Figure 3b). A silver grid was printed on three of these areas, whereas one slightly larger area was kept metal free for reflectance and external quantum efficiency (EQE) measurements. Current density–voltage (J–V) measurements were conducted on the cells with a Ag grid under 100 mW cm^{-2} (air mass 1.5 global, i.e., AM1.5G) illumination. Scanning electron microscope (SEM) images of the cross-section of the cell rear-contact show the nearly 75 nm Zn_xSi_yO layer deposited between the Si and the Ag layer (Figure 3c,d). Dark field TEM images, alongside elemental mapping, confirm the conformal coverage of the pyramids with the TCO layer containing ZnO:Al and SiO_2. A high-resolution TEM image of this layer is shown in Figure S4 of the Supporting Information confirms the presence of nanocrystals in the layer similar to Figure 1e.

Figure 4a displays the J–V characteristics of the most efficient cell that was made with ZnO:Al containing 8.6 mol% SiO_2 as rear-TCO. The cell produces a short-circuit current density (J_{SC}) of nearly 37.8 mA cm^{-2} and has 20.8% power conversion efficiency (PCE). All the cells produced with ZnO:Al containing up to 8.6 mol% SiO_2 show similar J–V characteristics. The cells produced with ZnO:Al containing 40 and 52 mol% SiO_2 display the J–V characteristics shown in Figure 4b, implying the presence of a large series resistance in the cell, likely to be caused by a contact resistivity issue.[22,34]

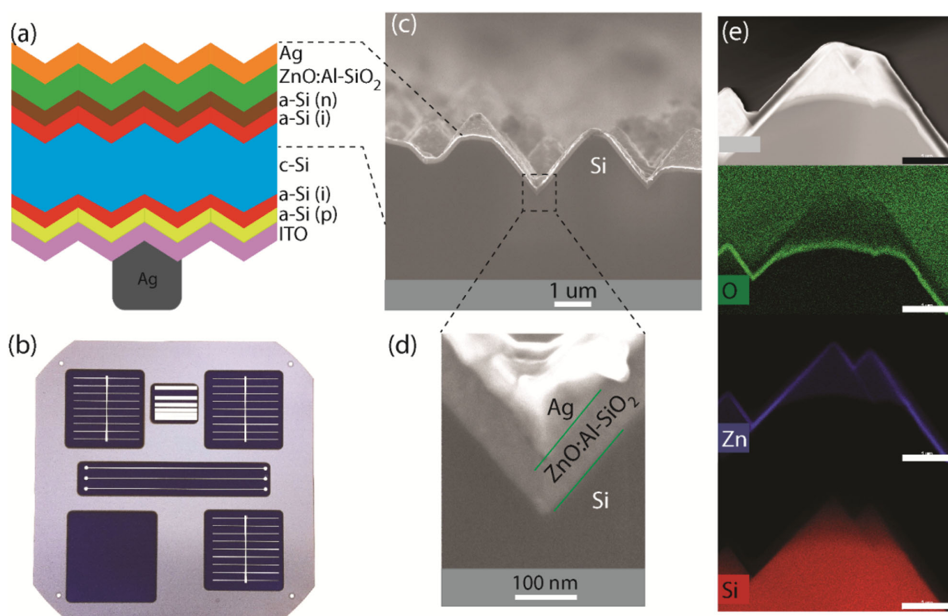

Figure 3. Si heterojunction solar cell structure. Panel a) shows the schematic of a c-Si heterojunction solar cells. Panel b) shows the digital photograph of the cells we produced in this work on 250-µm thick, 100 cm^2 Si wafer in which three areas each 4 cm^2 with metallic grid are used for J–V measurements and the larger area without the grid was used for EQE and reflectance measurement. Panels c) and d) show the cross-section SEM images of the cell back-contact which illustrate the ZnO:Al-SiO_2 layer and the Ag back contact. Panel e) shows from top to bottom the dark-field TEM image, along with O, Si, and Zn content map on the back contact of the cell. The scale bar is 1 µm.

© 2015 WILEY-VCH Verlag GmbH & Co. KGaA, Weinheim

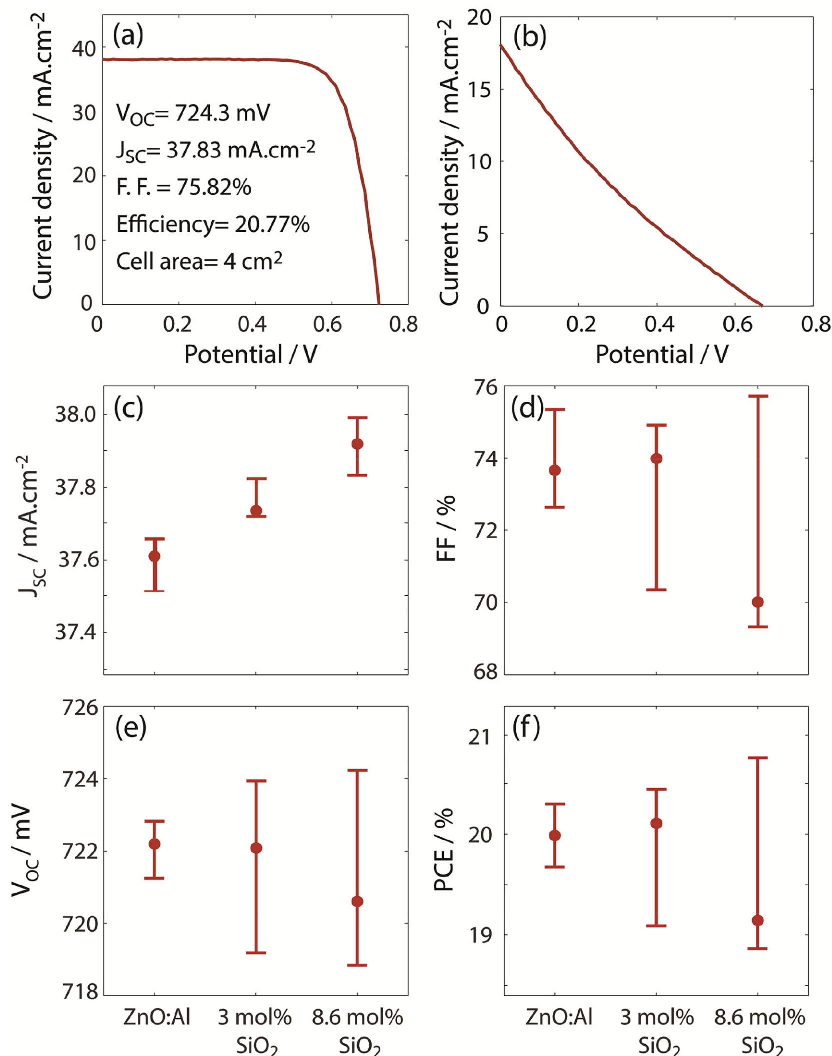

Figure 4. Photovoltaic characterization. Panel a) shows the *J–V* curve (under AM1.5G) of the most efficient SHJ cell produced using ZnO:Al with 8.6 mol% SiO_2. Panel b) shows the S-shaped *J–V* curves observed in the cells with ZnO:Al having 40 and 52 mol% SiO_2. Panels c–f) summarize the photovoltaic data of the cells measured under AM1.5G with different back-TCO compositions.

The average characteristics of the cells with different rear-TCOs show that with the addition of SiO_2 there is a consistent improvement in J_{SC} of all the cells. This observation confirms that the addition of SiO_2 has led to improved optical absorption in the cell. Other cell parameters, i.e., open-circuit voltage (V_{OC}), fill factor (FF), and PCE, do not show a significant variation however their statistical distribution become more spread as more SiO_2 is added.

The EQE of all the cells is quite representative for typical high-efficiency SHJ solar cells, with a significant loss at $\lambda < 600$ nm and a plateau with more than 95% efficiency up to 1020 nm, followed by rapidly decreasing efficiency down to nearly 1200 nm.[3] The loss at $\lambda < 600$ nm is partly due to the reflectance from the cell[33] and is partly due to the optical absorption losses in the p-type a-Si layer.[8] At $\lambda > 1020$ nm the EQE drops due to the i) high dissipation in the ITO layer, caused by free-carrier absorption, ii) incomplete optical absorption in c-Si, and iii) the parasitic optical absorption in the rear-contact, i.e., rear-TCO and Ag. In this wavelength range, the absorption of the Si becomes weak and therefore single-path optical absorption in the Si wafer is not significant. Therefore the light makes several passes within the Si wafer with the upper limit of optical absorption set by the statistical $4n^2$ limit.[35] In every other pass the light interacts with the rear-TCO and the rear Ag contact and therefore it is subject to optical losses in these two layers.

To make the effect of SiO_2 addition to ZnO:Al more pronounced in the performance of the SHJ cell, we calculate the enhancement in EQE relative to that of the reference cell (inset of **Figure** 5a). We observe consistently that as the amount of added SiO_2 increases, the EQE improves, particularly in the IR. The improvement in EQE of the device with ZnO:Al containing 8.6 mol% SiO_2 at $\lambda > 1050$ nm reaches 20% which is quite important for application of these devices as the bottom cell of tandem devices.[36]

The near absorption edge reflectance from the cells at $\lambda > 1050$ nm also gives a good indication of the losses in the cell rear-contact.[8] In fact, larger reflectance translates into smaller optical absorptance in the rear-contact. The reflectance spectra of Figure 4b shows that the near absorption edge reflectance from the cells improves by increasing the SiO_2 content of the rear-TCO. This observation, in combination with the EQE data, confirms that addition of SiO_2 to ZnO:Al improves cells J_{SC} and PCE due to reduction of parasitic absorption losses in the rear-contact of the cell.

3. Conclusion

The optoelectronic properties, i.e., transparency and refractive index, of ZnO:Al were tailored by adding controlled amounta of SiO_2. The obtained compound can be classified in two main categories: one with a low SiO_2 content and one with a large SiO_2 content. We found that at low SiO_2 contents up to 8.6 mol%, SiO_2 modifies the refractive index and quenches the free carriers of ZnO:Al hence it improves the infrared transparency of the ZnO:Al layer. This comes at the cost of deteriorating the layer lateral conductivity whereas the vertical conductivity remains sufficiently high for applications as the rear-contact of crystalline Si solar cells. In addition, we observe that the presence of low refractive index SiO_2 leads to ZnO:Al-based compounds with lower refractive index relative to the pristine ZnO, over the full wavelength range, and in the short wavelength

© 2015 WILEY-VCH Verlag GmbH & Co. KGaA, Weinheim

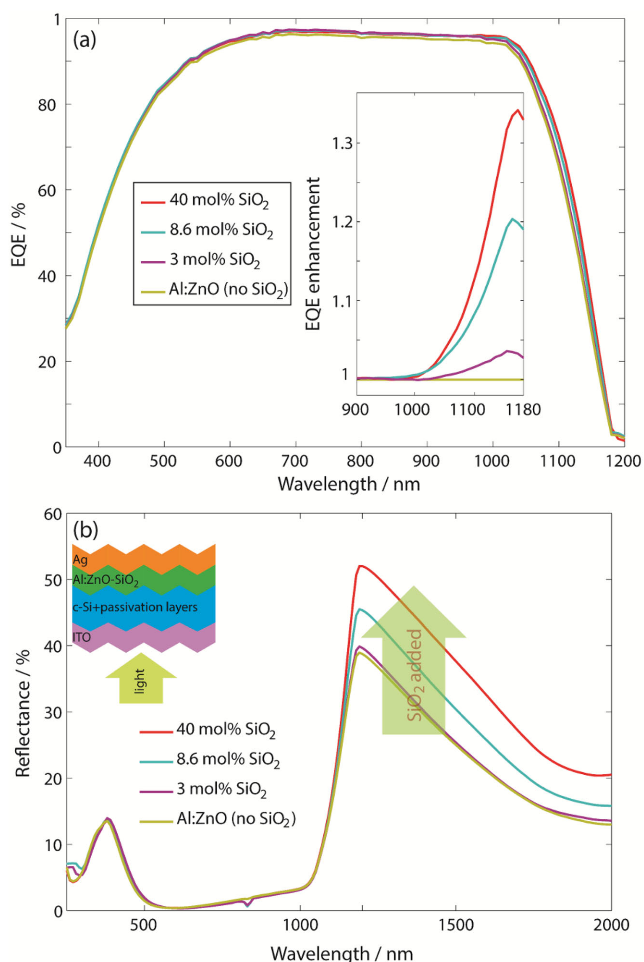

Figure 5. Spectral PV characterization. Panel a) shows the external quantum efficiency (EQE) and panel b) shows the reflectance spectra of the cells with rear-TCOs of different chemical composition.

range compared to the ZnO:Al. At high SiO_2 concentrations (40 mol% and higher) an amorphous mixture of ZnO:Al and SiO_2 forms with high transparency and low refractive index but with a large resistivity. These layers have proven useful in improving the short-circuit current density of Si heterojunction solar cells. We confirmed that this improvement is directly related to the reduction of parasitic plasmonic absorption losses in the rear-contact of the cell as the result of better transparency and lower refractive index obtained by adding optimal amounts of SiO_2 to ZnO:Al. In a broader perspective, our approach of adding the highly transparent and low refractive index SiO_2 to a TCO to modify its optoelectronic properties establishes a general strategy to further tailor the TCO for specific applications in LEDs and photovoltaics.

4. Experimental Section

TCO Deposition: The sputtering process was carried out in an Oerlikon Cluster line system. The system background pressure was 2×10^{-7} mbar and the depositions were conducted in a chamber equipped with four sputtering targets at typical pressures of 1–3 μbar obtained with 20 and 1.4 sccm of Ar and 95%Ar–5%O_2 gas flows, respectively. All the depositions reported in this work were conducted under these conditions. The substrate was rotated at 15 rpm to acquire a homogeneous thickness distribution of the layer. The structural, optical, and electrical characterizations were carried out on samples deposited on 1 mm thick Schott glass. The samples for ellipsometry were prepared on polished Si wafers with 100 nm dry oxide coating.

Cell Preparation: High quality n-type float zone (FZ) c-Si (100) wafers with a resistivity of 1–5 Ω cm^{-1} were used. The wafers were randomly textured in potassium hydroxide (KOH) solution and subsequently wet-chemically cleaned and dipped in hydrofluoric acid (HF) before layer deposition. Intrinsic a-Si:H layers were deposited on both sides of the wafers using plasma-enhanced chemical vapor deposition (PECVD). The p- and n-type a-Si:H layers were deposited on the front and back of the cell to form the emitter and back surface field. Indium tin oxide layers were sputtered on the front side of the wafers, whereas at the back side ZnO:Al and SiO_2 TCO with different chemical compositions was co-sputtered. The cells were finished with a sputtered silver reflector and a screen-printed silver front electrode grid. After screen printing the cells were annealed at 200 °C on a belt furnace for 20 min. Further details about the fabrication process can be found elsewhere.[37]

Characterizations: UV–vis spectrometry was conducted on lambda-950 equipment (Perkin Elmer). Spectroscopic ellipsometry was carried out using a Uvisel equipment of Horiba Jobin Yvon. The fitting was carried out using WinSE software. Hall-effect measurements were carried out using an HMS-5000 equipment. A Lucas Lab tool was used for 4-point-probe measurement of sheet resistance. SEM was conducted using an EOL JSM-7500TFE equipment at 2–10 keV beam energies. Photovoltaic characterization was carried out using a WXS-220S-L2 (WACOM) Super solar simulator. The EQE was measured using a IQE-scan (PVtools) equipment. TEM sample preparation was performed by mechanical polishing in a wedge configuration, followed by a final ion milling until electron transparency (Gatan PIPS ion miller). TEM observations were performed on an FEI Tecnai Osiris at the Center for Electron Microscopy of EPFL. The latter was also used for energy dispersive X-ray (EDX) mapping using Super-X silicon drift detectors in scanning TEM (STEM) mode. XPS was carried out using a Kratos AXSI Ultra piece of equipment with 100 meV steps. The measured XPS were fitted with the components of the Gaussian–Lorentzian product using Multipak software.

Supporting Information

Supporting Information is available from the Wiley Online Library or from the author.

Acknowledgements

The authors thank Lorenzo Fanni for XRD measurement, Danièle Laub and Colette Vallotton from CIME of EPFL for TEM sample preparation. The authors thank PV-Center of CSEM for preparing textured crystalline Si wafers. This work was financially supported by the CCEM-CH under the CONNECT PV project, the SNSF under the "PV2050" project of the PNR70 program "Energy Turnaround" and the "Synergy" Nano-tera.ch RTD project, by the Swiss Federal Office of Energy under Grant No. SI/501072-01, the European Commission's FP7 Program under the Hercules (Contract No. 608498) and the CHEETAH (Contract No. 609788) projects, and the DOE under the FPaceII project.

Received: August 23, 2015
Revised: October 14, 2015
Published online: November 19, 2015

[1] K. Ellmer, *Nat. Photonics* **2012**, *6*, 809.
[2] K. Masuko, M. Shigematsu, T. Hashiguchi, D. Fujishima, M. Kai, N. Yoshimura, T. Yamaguchi, Y. Ichihashi, T. Mishima, N. Matsubara, T. Yamanishi, T. Takahama, M. Taguchi, E. Maruyama, S. Okamoto, *IEEE J. Photovoltaics* **2014**, *4*, 1433.

© 2015 WILEY-VCH Verlag GmbH & Co. KGaA, Weinheim

FULL PAPER

[3] S. De Wolf, A. Descoeudres, Z. C. Holman, C. Ballif, *Green* **2012**, *2*, 7.
[4] J. Chen, L. Lu, W. Wang, *J. Phys. Chem. C* **2012**, *116*, 10841.
[5] a) X. Sheng, M. H. Yun, C. Zhang, A. a. M. Al-Okaily, M. Masouraki, L. Shen, S. Wang, W. L. Wilson, J. Y. Kim, P. Ferreira, X. Li, E. Yablonovitch, J. A. Rogers, *Adv. Energy Mater.* **2015**, *5*, 1400919; b) B. Niesen, N. Blondiaux, M. Boccard, M. Stuckelberger, R. Pugin, E. Scolan, F. Meillaud, F. J. Haug, A. Hessler-Wyser, C. Ballif, *Nano Lett.* **2014**, *14*, 5085.
[6] S. Reineke, M. Thomschke, B. Lüssem, K. Leo, *Rev. Mod. Phys.* **2013**, *85*, 1245.
[7] a) Z. C. Holman, S. De Wolf, C. Ballif, *Light: Sci. Appl.* **2013**, *2*, e106; b) Z. C. Holman, M. Filipič, B. Lipovšek, S. De Wolf, F. Smole, M. Topič, C. Ballif, *Sol. Energy Mater. Sol. Cells* **2014**, *120*, 426.
[8] Z. C. Holman, A. Descoeudres, S. De Wolf, C. Ballif, *IEEE J. Photovoltaics* **2013**, *3*, 1243.
[9] Z. C. Holman, M. Filipič, A. Descoeudres, S. De Wolf, F. Smole, M. Topič, C. Ballif, *J. Appl. Phys.* **2013**, *113*, 013107.
[10] M. Morales-Masis, S. Martin De Nicolas, J. Holovsky, S. De Wolf, C. Ballif, *IEEE J. Photovoltaics* **2015**, *5*, 1340.
[11] E. Chong, Y. S. Chun, S. Y. Lee, *Appl. Phys. Lett.* **2010**, *97*, 102102.
[12] A. K. Das, R. S. Ajimsha, L. M. Kukreja, *J. Appl. Phys.* **2014**, *115*, 193705.
[13] a) J. Clatot, G. Campet, A. Zeinert, C. Labrugère, M. Nistor, A. Rougier, *Sol. Energy Mater. Sol. Cells* **2011**, *95*, 2357; b) J. T. Luo, X. Y. Zhu, G. Chen, F. Zeng, F. Pan, *Appl. Surf. Sci.* **2012**, *258*, 2177; c) N. Rashidi, V. L. Kuznetsov, J. R. Dilworth, M. Pepper, P. J. Dobson, P. P. Edwards, *J. Mater. Chem. C* **2013**, *1*, 6960; d) I. Sorar, D. Saygin-Hinczewski, M. Hinczewski, F. Z. Tepehan, *Appl. Surf. Sci.* **2011**, *257*, 7343; e) H.-C. Wu, Y.-C. Peng, T.-P. Shen, *Materials* **2012**, *5*, 2088.
[14] J. F. Watts, J. Wolstenholme, *An Introduction to Surface Analysis by XPS and AES*, John Wiley & Sons, Ltd., New York, **2003**.
[15] F. J. Himpsel, F. R. McFeely, A. Taleb-Ibrahimi, J. A. Yarmoff, G. Hollinger, *Phys. Rev. B* **1988**, *38*, 6084.
[16] C. Faure, J. Clatot, L. Teulé-Gay, G. Campet, C. Labrugère, M. Nistor, A. Rougier, *Thin Solid Films* **2012**, *524*, 151.
[17] A. Dabirian, Y. Kuzminykh, B. Afra, S. Harada, E. Wagner, C. S. Sandu, G. Benvenuti, S. Rushworth, P. Muralt, P. Hoffmann, *Electrochem. Solid-State Lett.* **2010**, *13*, G60.
[18] A. Dabirian, Y. Kuzminykh, S. C. Sandu, S. Harada, E. Wagner, P. Brodard, G. Benvenuti, S. Rushworth, P. Muralt, P. Hoffmann, *Cryst. Growth Des.* **2011**, *11*, 203.
[19] G. Lucovsky, G. B. Rayner, *Appl. Phys. Lett.* **2000**, *77*, 2912.
[20] D. A. Neumayer, E. Cartier, *J. Appl. Phys.* **2001**, *90*, 1801.
[21] D. Song, A. G. Aberle, J. Xia, *Appl. Surf. Sci.* **2002**, *195*, 6.
[22] L. Lu, J. Chen, L. Li, W. Wang, *Nanoscale Res. Lett.* **2012**, *7*, 293.
[23] a) N. Mitoma, S. Aikawa, X. Gao, T. Kizu, M. Shimizu, M.-F. Lin, T. Nabatame, K. Tsukagoshi, *Appl. Phys. Lett.* **2014**, *104*, 102103; b) J. W. Hennek, J. Smith, A. Yan, M. G. Kim, W. Zhao, V. P. Dravid, A. Facchetti, T. J. Marks, *J. Am. Chem. Soc.* **2013**, *135*, 10729.
[24] H. Peelaers, E. Kioupakis, C. G. Van de Walle, *Appl. Phys. Lett.* **2012**, *100*, 011914.
[25] M. Fox, *Optical Properties of Solids*, Oxford University Press Inc., New York **2010**.
[26] L. Lu, J. Chen, W. Wang, *Appl. Phys. Lett.* **2013**, *103*, 123902.
[27] M. Hála, S. Fujii, A. Redinger, Y. Inoue, G. Rey, M. Thevenin, V. Deprédurand, T. P. Weiss, T. Bertram, S. Siebentritt, *Prog. Photovoltaics: Res. Appl.* **2015**, *23*, 1630.
[28] a) A. Frölich, M. Wegener, *Opt. Mater. Express* **2011**, *1*, 7; b) Q. H. Li, D. Zhu, W. Liu, Y. Liu, X. C. Ma, *Appl. Surf. Sci.* **2008**, *254*, 2922.
[29] a) M. Berginski, J. Hüpkes, W. Reetz, B. Rech, M. Wuttig, *Thin Solid Films* **2008**, *516*, 5836; b) I. Volintiru, M. Creatore, M. C. M. van de Sanden, *J. Appl. Phys.* **2008**, *103*, 033704; c) C. Guillén, J. Herrero, *Vacuum* **2010**, *84*, 924.
[30] W. L. Bond, *J. Appl. Phys.* **1965**, *36*, 1674.
[31] J. C. Maxwell Garnett, *Philos. Trans. R. Soc. London, B* **1906**, *205*, 237.
[32] I. H. Malitson, *J. Opt. Soc. Am.* **1965**, *55*, 1205.
[33] Z. C. Holman, A. Descoeudres, L. Barraud, F. Z. Fernandez, J. P. Seif, S. De Wolf, C. Ballif, *IEEE J. Photovoltaics* **2012**, *2*, 7.
[34] B. Demaurex, J. P. Seif, S. Smit, B. Macco, W. M. M. E. Kessels, J. Geissbuhler, S. De Wolf, C. Ballif, *IEEE J. Photovoltaics* **2014**, *4*, 1387.
[35] E. Yablonovitch, *J. Opt. Soc. Am.* **1982**, *72*, 899.
[36] P. Löper, S.-J. Moon, S. Martín de Nicolas, B. Niesen, M. Ledinsky, S. Nicolay, J. Bailat, J.-H. Yum, S. De Wolf, C. Ballif, *Phys. Chem. Chem. Phys.* **2015**, *17*, 1619.
[37] A. Descoeudres, Z. C. Holman, L. Barraud, S. Morel, S. De Wolf, C. Ballif, *IEEE J. Photovoltaics* **2013**, *3*, 83.

© 2015 WILEY-VCH Verlag GmbH & Co. KGaA, Weinheim